This article has been accepted for publication in IEEE Access. This is the author's version which has not been fully edited and content may change prior to final publication. Citation information: DOI 10.1109/ACCESS.2024.3404410

Date of publication xxxx 00, 0000, date of current version xxxx 00, 0000.

Digital Object Identifier 10.1109/ACCESS.2022.Doi Number

Mechanical and Vibration Analysis of a High-Speed Outer Rotor Electric Motor

Himel Barua, Lianshan Lin, Vandana Rallabandi, Jon Wilkins, Praveen Kumar, Burak Ozpineci
Oak Ridge National Laboratory, Oak Ridge, TN 37830 USA

Corresponding author: Himel Barua (e-mail: baruah@ornl.gov).

This work was supported by the US Department of Energy (DOE) Vehicle Technologies Office's Electric Drive Technologies Program.

ABSTRACT This study explores the design and engineering of high-speed outer rotor electric motors, focusing on addressing the unique challenges these motors face for integrated drive applications. Outer rotor motors are preferred in applications requiring high power density and compact design. They enable efficient use of space by integrating power electronics within the motor structure, a critical advantage over traditional inner rotor designs. However, the adoption of high-speed outer rotor motors introduces several technical challenges, including managing increased mechanical stresses, ensuring dynamic balance, mitigating vibrations, and the need for specialized bearings capable of supporting high operational speeds. To tackle these issues, the study proposes a novel design framework that includes two configurations: a cantilevered design and a design supported at both ends. A significant innovation within this framework is the use of a C-fiber-based sleeve around the rotor. This sleeve preloads the magnets and the rotor structure, enhancing the motor's mechanical integrity and allowing it to operate safely at speeds up to 20,000 rpm. The study employs finite element analysis for structural and modal assessments alongside rotodynamic studies to evaluate the proposed designs. These analyses are crucial for understanding the vibrational behavior and stability of the motor under operational conditions. Based on these evaluations, the study presents specific recommendations to improve the rotodynamic performance of the motors, focusing on aspects such as balancing and vibration reduction

INDEX TERMS Electric motor, natural frequency, permanent magnet, rotodynamic, spin analysis

I. INTRODUCTION

High-speed permanent magnet (PM) motors stand out for their efficiency and compact design in electric motors. These motors, which are vital in electric vehicles, industrial machinery, and renewable energy applications, use PMs to generate motion. Among these motors, outer rotor PM motors, in which the rotor encircles the stator, are particularly recognized for their higher torque density than traditional inner rotor designs. This configuration is advantageous for various applications, from electric vehicles to industrial tools, making studying its design and performance crucial for technological advancements [1], [2]. In outer rotor motors, surface-mounted permanent magnets (SPMs) can provide higher torque density than regular PMs [3]. Examples of recent work on outer rotor motors include [4], which investigates the effect of axial length over pitch-pole ratio in outer rotor brushless DC (BLDC) motors, and [5], which reports on the design and optimization of hub BLDC motors.

Although outer rotor SPM motors are used in aerospace, ground, and light-transportation applications [6], [7], [8], the maximum motor speed is limited to 15,000 rpm [2] because of mechanical constraints. At high speeds, the major mechanical concerns for electric motors are tip speed (linear velocity of the rotor surface) [9], stress in the rotor structure, temperature, and resonant frequency [10]. In SPM designs, PMs cannot sustain large centrifugal force because of their lower tensile strength [11]. One significant challenge for high-speed outer rotor SPM motors is retaining the magnets at the high-speed operating condition. Chu et al. [12] developed a 2D analytical method to perform structural analyses for inner rotor motors. Nagaoka, Takemoto, and Ogasawara [13] developed a 2D finite element analysis (FEA) model for surface-mounted inner rotor motors and studied the effects of gaps between the magnets. Barrans et al. [14] and Schubert and Sarlioglu [15] developed FEA models to study the effect of stresses in SPMs on inner rotor motors.

US DRIVE 2025 [16] set technical targets of 33 kW/L for electric-drive power density, 50 kW/L for electric motors, and 100 kW/L for inverters. To reach these targets, an outer rotor design in which the inverter is placed inside the stator was proposed. The cooling channels for the stator are placed inside the winding slot. Because of the placement of the inverter inside the stator, a large-diameter stator and outer rotor were chosen. At 20,000 rpm, the rotor and surface-mounted magnets are subjected to very high stress. The interaction of magnetic force between the stator and rotor and the high speed of the rotor creates mechanical vibration which can cause

This manuscript has been authored by UT-Battelle, LLC, under contract DE-AC05-00OR22725 with the US Department of Energy (DOE). The US government retains and the publisher, by accepting the article for publication, acknowledges that the US government retains a nonexclusive, paid-up, irrevocable, worldwide license to publish or reproduce the published form of this manuscript, or allow others to do so, for US government purposes. DOE will provide public access to these results of federally sponsored research in accordance with the DOE Public Access Plan (http://energy.gov/downloads/doe-public-access-plan).

This work is licensed under a Creative Commons Attribution-NonCommercial-NoDerivatives 4.0 License. For more information, see https://creativecommons.org/licenses/by-nc-nd/4

This article has been accepted for publication in IEEE Access. This is the author's version which has not been fully edited and content may change prior to final publication. Citation information: DOI 10.1109/ACCESS.2024.3404410

damage not only to motor components but also to the inverter. This design constraint made the mechanical design complicated.

As interest in high-speed SPM motors has increased, researchers have been attracted to stress research on the retaining sleeve, a key component to ensure the safety and stability of the SPM motor rotor [17]. Fiber-reinforced composite materials have high specific strength, high specific modulus, and low eddy current loss, making them good candidates for retaining sleeves in high-speed SPM motors. The finite element method (FEM) has been used to verify that a disc-shaped PM rotor can work up to 200,000 rpm with a C-fiber enclosure [18]. A high-speed PM machine with segmented magnets retained by a C-fiber sleeve was prototyped and tested at 90,000 rpm [19]. The rotor stability indirectly indicated the validity of the theoretical analysis and design scheme. Zhang et al. [2] developed a retaining sleeve that can work in megawatt PM machines at high speeds of 22,000 rpm. Sanchez et al. [3] discussed the limits of high-speed inner rotor PM motor designs, the dynamic stability limit of PM motors, and how the dynamic stability is related to rotor geometry. Yu et al. [20] performed rotodynamic analysis for a cantilever outer rotor motor with very high tip speeds and analyzed the modes of vibration. Schubert and Sarlioglu [13] performed mechanical analyses for various inner rotor designs and compared Campbell diagrams for each design. They also studied the rotodynamic behavior of the rotor-bearing structure and studied the different modes of vibration. Chen et al. [5] and Balachandran et al. [21] studied high-speed outer rotor motors and their mechanical challenges; in each of these studies, the rotor was balanced by bearings on both sides. Numerous rotodynamic analyses for inner rotor motors are available in the literature [22], [23], [24], but few such analyses have been performed for high-speed outer rotor PM motors. Several studies report on the electromagnetic design and performance of outer rotor motors, but few discuss the mechanical design and assembly.

The work reported in this paper attempts to bridge this gap. This work presents a detailed FEA-based mechanical analysis which was performed to compare two rotor designs with a peak operating speed of 20,000 rpm. Section II discusses the mechanical design and model development, and section III discusses the spin analysis at rated speed and peak speed. Section IV discusses the results, section V discusses the vibration analysis, and sections VI, VII, and VIII discuss the forced frequency analysis, rotodynamic analysis of the rotor structure, and validation of the rotor natural frequency and Campbell diagrams with FEA results and experimental results, respectively. Section IX discusses general design guidelines. The final section discusses the conclusion and the future direction of this work.

II. MECHANICAL DESIGN AND MODEL DEVELOPMENT

This study analyzed a permanent magnet synchronous motor (PMSM) as part of an integrated drive system. To accommodate the inverter within the stator, an outer rotor motor design was required with magnets placed on the inner surface of the rotor. The motor had a rated power of 55 kW and a peak power of 100 kW. Fig. 1 shows a diagram of the inverter and motor. A three-phase half-bridge segmented inverter [25] was selected and supplied a sinusoidal current to the motor. An outer rotor design was chosen for the motor to accommodate the inverter in the stator bore. The PMSM rotor had a 16-pole Halbach array with 4 magnet segments per pole fixed to the inner surface of the back iron. The back iron was made of laminated steel with a thickness of 3 mm. Table I gives the key motor specifications.

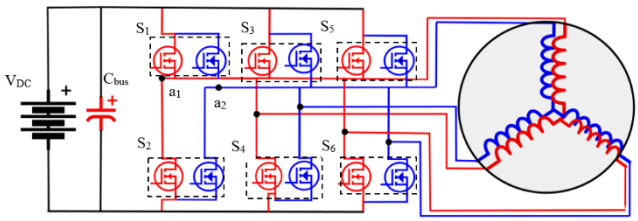

FIGURE 1. Schematic of the six-phase inverter and motor.

TABLE I
MOTOR SPECIFICATIONS

Parameter	Value
Continuous power (kW)	55
Peak power (kW)	100
Maximum speed (rpm)	20,000
Battery voltage (V_{DC})	650
Power factor	>0.8
Maximum current (A)	600
Maximum efficiency (%)	>97
Torque ripple (%)	5
Number of stator slots	18
Number of rotor poles	16
Air gap length (mm)	2
Stack length (mm)	44
Outer diameter (mm)	250
Permanent magnet height (mm)	12

Table II [26] presents the material properties of different layers of the rotor. The rotor frame was made of high-strength steel with a yield limit of 800 MPa. The dysprosium-free magnets (N50) were made of neodymium, which had a highly anisotropic mechanical property. The neodymium could sustain a compressive load up to 1,100 MPa and a tensile load up to 74 MPa [27] [28]. This posed some mechanical challenges, especially at peak speed.

TABLE II
MATERIAL PROPERTIES

Component	Material	Density	Elastic modulus	Poisson's	Shear modulus	Yield strength

This work is licensed under a Creative Commons Attribution-NonCommercial-NoDerivatives 4.0 License. For more information, see https://creativecommons.org/licenses/by-nc-nd/4

This article has been accepted for publication in IEEE Access. This is the author's version which has not been fully edited and content may change prior to final publication. Citation information: DOI 10.1109/ACCESS.2024.3404410

		(kg/m^3)	(GPa)			ratio			(Gpa)			(MPa)
Rotor frame	Steel	7,850	193			0.27			—			800
PM	Magnet	7,500	170			0.31			—			74 (Tension) 1,100 (Compression)
Inner sleeve	C fiber	1,360	172			0.45			—			—
C-fiber sleeve	C fiber	1,360	*xx*	*yy*	*zz*	*xy*	*xz*	*yz*	*xy*	*xz*	*yz*	3,087
			146	126	126	0.31	0.31	0.31	4.7	4.5	4.7	

TABLE III
PERFORMANCE OF THE MOTOR UNDER DIFFERENT OPERATING CONDITIONS

Operating condition	Speed (rpm)	Power (kW)	Current (A)	RMS line voltage (V)	Cu loss (W)	Core loss (W)	Magnet Loss (W)	Efficiency (%)
Rated power	6,667	62	194	197	699	815	27	97.6
Peak	6,667	120	388	213	2,798	855	31	97.0
Max speed	20,000	59	194	463	699	3,649	145	92.9

There were four magnet segments per pole. Generally, the pole-arc coefficient of Halbach-array magnets is maintained at 1 [31], [37]. Fig. 2(a) shows the motor cross section showing the rotor and PM directions. Table III shows the performance of the motor at various operating conditions.

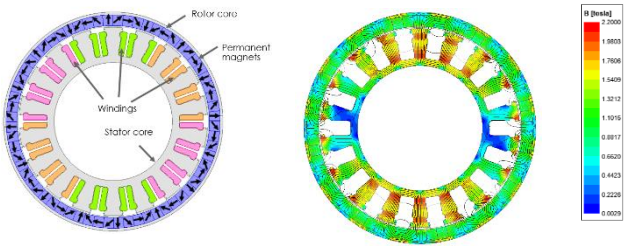

(a) (b)

FIGURE 2. (a) Cross-sectional view of the motor and (b) flux distribution through the cross section.

Fig. 3(a) shows a 3D view of the motor structure with the steel outer casing, and Fig. 3(b) shows a cross-sectional view of the motor. The total length was 315 mm, with three supports. Inside the stator, a steel casing was added to accommodate the inverter, which contained six power modules with heat sinks. A slot heat exchanger was used to cool the motor, which was placed in between the slots. The heat exchanger was made of AlN.

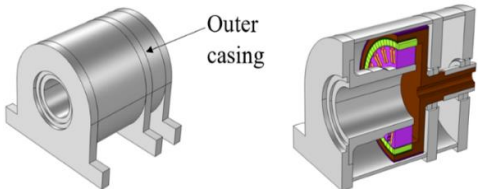

(a) (b)

FIGURE 3. (a) 3D full-scale and (b) cross-sectional views of the motor for the cantilever rotor design

Fig. 4(a) and (b) display the construction of the cantilever and simply supported rotors. Table IV presents the dimensions of both motors. In the cantilever design, the rotor shaft was positioned in two sets of angular contact bearings (four pieces), each having a width of 13 mm and a bore diameter of 60 mm, on one side of the rotor structure. The bearings were spaced 55 mm apart. On the other hand, the simply supported design had one set of bearings (two pieces) on each side of the rotor structure. The bearings were composed of 32 ceramic (Si_3N_4) balls, which provided electrical isolation between the inner race and outer race of the bearings.

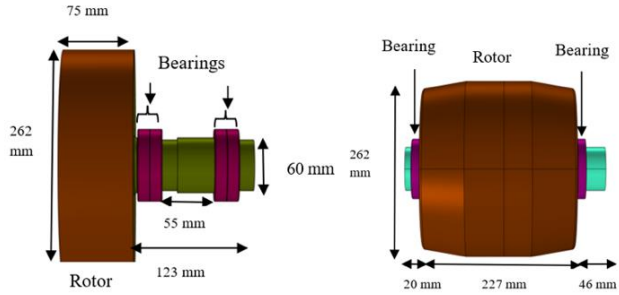

(a) (b)

FIGURE 4. (a) Cantilever design and (b) simply supported design.

This work is licensed under a Creative Commons Attribution-NonCommercial-NoDerivatives 4.0 License. For more information, see https://creativecommons.org/licenses/by-nc-nd/4

This article has been accepted for publication in IEEE Access. This is the author's version which has not been fully edited and content may change prior to final publication. Citation information: DOI 10.1109/ACCESS.2024.3404410

TABLE IV
MOTOR DESIGN DIMENSIONS [29]

	Cantilever design	Simply supported design
Rotor outer diameter (mm)	264	264
Rotor inner diameter (mm)	242	221
Rotor length (mm)	75	227
Shaft outer diameter (mm)	60	60
Shaft length (mm)	123	20
Stator outer diameter (mm)	208	208
Stator inner diameter (mm)	130	130
Magnet height (mm)	12	12
Magnet width (mm)	10	10
Volume (L)	2.32	4.89
Weight (kg)	17	37

III. STATIC STRUCTURAL ANALYSIS (SPIN ANALYSIS)

COMSOL, an FEA software, was used for the spin analysis. The geometry was prepared in SOLIDWORKS, and all other FEA pre- and postprocessing as well as the solution were done in COMSOL. The first step was to conduct the static analysis of the rotor at the rated speed (6,666 rpm) and peak speed (20,000 rpm). The equilibrium equation [30] of any elastic body with a rotating body force is

$$\sigma_h - \sigma_r - \frac{r d\sigma_r}{dr} = \rho r^2 \omega^2, \tag{1}$$

where σ_h is hoop stress, σ_r is radial stress, ω is rotational speed (rad/s), and ρ is density. The corresponding constitutive and compatibility equations are

$$\begin{Bmatrix} \epsilon_r \\ \epsilon_h \end{Bmatrix} = \left(\frac{1}{E}\right) \begin{bmatrix} 1 & -\nu \\ -\nu & 1 \end{bmatrix} \begin{Bmatrix} \sigma_r \\ \sigma_h \end{Bmatrix} \tag{2}$$

and

$$\frac{r d\epsilon_r}{dr} - \frac{d}{dr}\left(\frac{r^2 d\epsilon_h}{dr}\right) = 0, \tag{3}$$

where ϵ_r is radial strain, ϵ_h is hoop strain, ν is Poisson's ratio, and E is modulus of elasticity. Equation (1) states that the force generated by rotation is directly proportional to the rotational speed, following a second-order polynomial relationship. As the speed and force increase, the stress generated in the rotating body (known as hoop stress) also increases. The ability of the rotating components to withstand this stress depends on their strength. To prevent failure, the components must have a higher yield strength than the hoop stress generated due to rotation, or a compressive force must be applied to balance the outward centrifugal force.

IV. RESULTS

A. STRUCTURAL ANALYSIS AT RATED AND PEAK SPEED

Hoop stress is a type of mechanical stress that occurs when a force is applied circumferentially (perpendicular to the axis) to a cylindrical or spherical object, such as the rotor of an electric motor (E-motor). In the context of an E-motor rotor, hoop stress refers to the stress experienced by the cylindrical rotor due to the rotational forces acting on it. Fig. 5(a) shows the hoop stress in the outer rotor and all the components for the cantilever design, and Fig. 5(b) shows the hoop stress for the simply supported design at the rated speed, 6,666 rpm. The maximum hoop stress in the rotor body and magnet array at peak speed are shown in Fig. 5(c) and 5(d). In this figure, positive values refer to tensile stress and negative values to compressive stress. The stresses at rated and peak speeds for both rotor designs are presented in Table V. Because the stress due to rotor rotation is tensile in nature, the magnets would not be able to sustain the stress.

TABLE V
HOOP STRESS IN THE ROTOR AND MAGNETS FOR DIFFERENT SPEEDS WITHOUT THE C-FIBER SLEEVE

	Stress in cantilever design (MPa)		Stress in simply supported design (MPa)	
	Rotor	Magnets	Rotor	Magnets
6,666 rpm	67	55	58.7	38.1
20,000 rpm	754	600	653	424

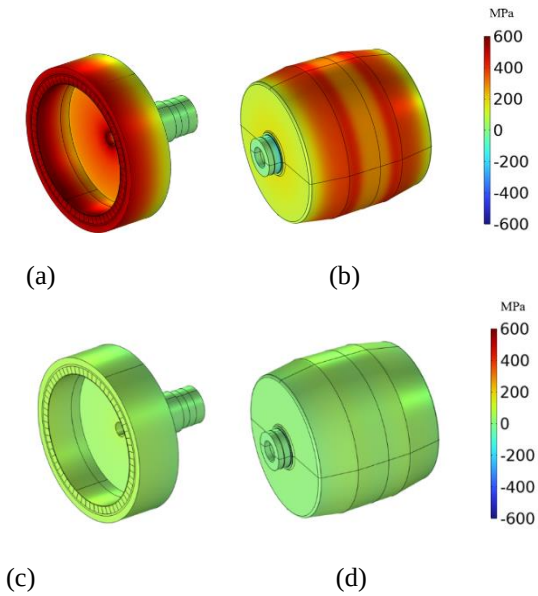

FIGURE 5. Hoop stress without the sleeve at the rated speed (6,666 rpm) for (a) the cantilever design and (b) the simply supported design and at the peak speed (20,000 rpm) for (c) the cantilever design and (d) the simply supported design.

To withstand the tensile stress produced by centrifugal force, both rotor designs required a C-fiber sleeve on their outer surfaces. This sleeve provided a compressive load on the outer surface, acting inward radially to balance the outward centrifugal force. A numerical study was conducted to determine the required contact pressure to sustain the centrifugal force at peak speed. The study showed that the C-fiber sleeve must apply at least 100 MPa compressive pressure to keep the magnet tensile stress lower than 74 MPa. Fig. 6 illustrates the relationship between the hoop stress at the rotor and magnets and the contact pressure at the outer surface for the cantilever design. For the simply supported design,

This work is licensed under a Creative Commons Attribution-NonCommercial-NoDerivatives 4.0 License. For more information, see https://creativecommons.org/licenses/by-nc-nd/4

This article has been accepted for publication in IEEE Access. This is the author's version which has not been fully edited and content may change prior to final publication. Citation information: DOI 10.1109/ACCESS.2024.3404410

100 MPa contact pressure is sufficient to keep the magnets within the yield strength limit.

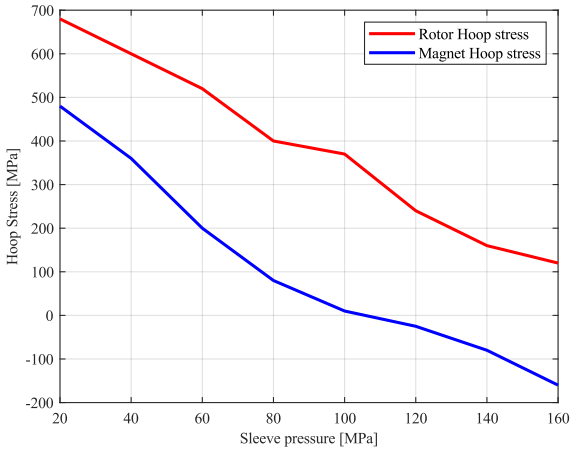

FIGURE 6. Contact pressure required by the C-fiber sleeve at the outer surface of the rotor.

Fig. 7 shows the stress at the magnets for the cantilever rotor at 20,000 rpm before and after the sleeve was used. Before the sleeve preload, the stress in the magnets was close to 500 MPa, whereas with sleeve preload it reduced to 20 MPa tensile stress and 50 MPa compressive stress. Fig. 8 shows the hoop stress in the outer rotor surface for both rotor designs at peak speed.

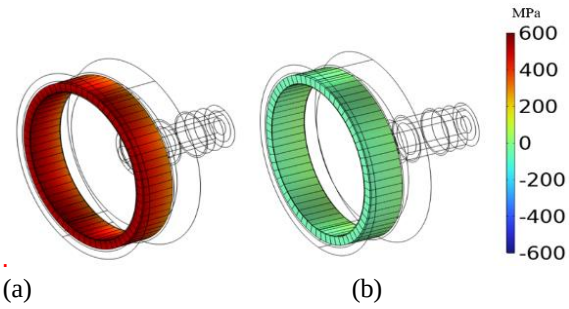

FIGURE 7. Hoop stress at the magnet array at 20,000 rpm (a) without the sleeve and (b) with the sleeve.

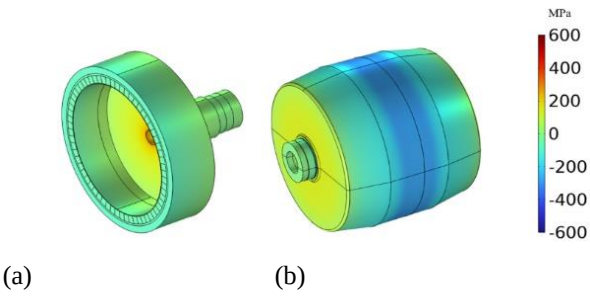

FIGURE 8. Hoop stress at peak speed with preload for (a) the cantilever design and (b) the simply supported design.

Each rotor design showed a different stress distribution at the outer rotor surface, as shown in Fig. 9 for the cantilever design and in Fig. 10 for the simply supported design. In the cantilever design, the maximum stress occurred at the free end. Fig. 9 shows that without preload applied, all the stress was tensile in nature, whereas with the C-fiber sleeve applying a preload of 100 MPa, the stress was compressive in nature. Fig. 10 shows the same trend. At the middle section of the rotor, without preloading, the stress was the highest compared with rest of the rotor, whereas with preloading, the stress was lowest at the middle section, as shown by the valleys and peaks in Fig. 10.

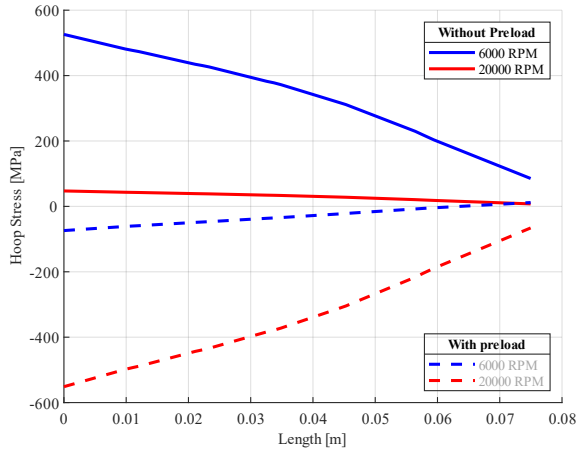

FIGURE 9. Stress distribution at the outer surface of the cantilever rotor.

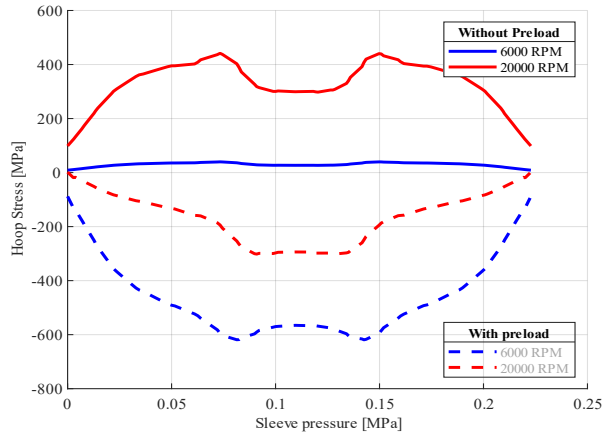

FIGURE 10. Stress distribution at the outer surface of the simply supported rotor.

Fig. 11 shows that with the C-fiber sleeve around the rotor and assuming 100 MPa compressive stress, the displacements of the outer rotors would be kept to less than 0.04 mm. At 6,000 rpm, the sleeve pressure would be less than 100 MPa because the corresponding centrifugal force would be less. Fig. 12 shows that keeping the compressive pressure between 20 and 40 MPa would be enough to balance the centrifugal force at 6,000 rpm.

This work is licensed under a Creative Commons Attribution-NonCommercial-NoDerivatives 4.0 License. For more information, see https://creativecommons.org/licenses/by-nc-nd/4

This article has been accepted for publication in IEEE Access. This is the author's version which has not been fully edited and content may change prior to final publication. Citation information: DOI 10.1109/ACCESS.2024.3404410

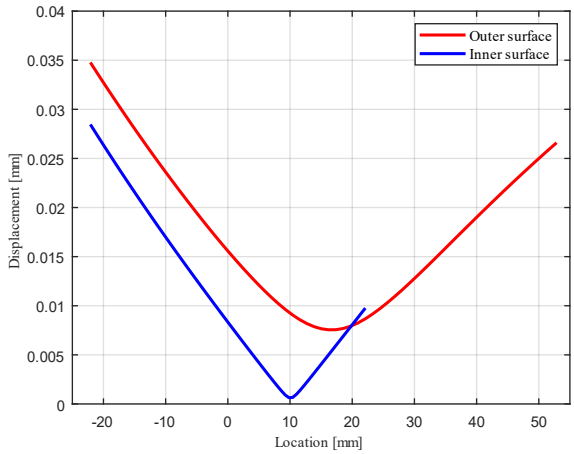

FIGURE 11. Displacements at the outer and inner surfaces of the rotor with the sleeve at 20,000 rpm (Cantilever design).

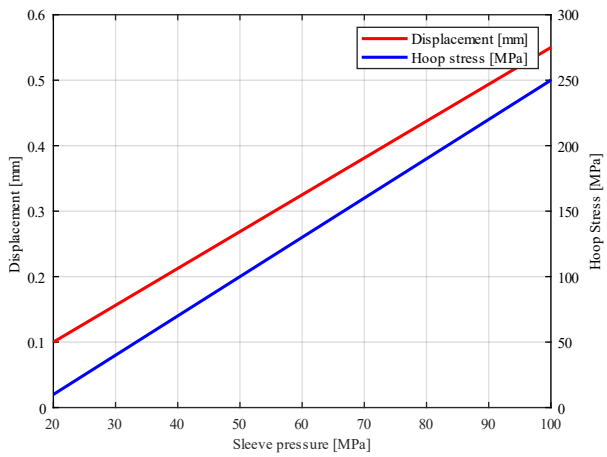

FIGURE 12. Displacement and hoop stress at the outer rotor with different sleeve pressures at 6,000 rpm.

B. EFFECT OF ADHESIVE AT OUTER ROTOR AND MAGNET INTERFACE

In an SPM design, magnets are placed on the surface of the outer rotor instead of being embedded within it. In the present design, magnet arrays were placed on the surface of the laminated back iron, which was positioned on the inner surface of the outer rotor. The strength of the adhesive used to keep the magnet arrays in place with the other components is crucial. Numerical simulations were performed to observe the effect of adhesive strength on rotating conditions. Structural adhesives available in the market have tensile strengths close to 40 MPa, whereas shear strengths vary from 2 to 17 MPa. The epoxy's modulus of elasticity is 3.2 GPa, and the Poisson's ratio is 0.3. The model considered two extreme cases: case A, with a shear strength of 17 MPa, and case B, with a shear strength of 2 MPa. The results showed that with the sleeve wrapped around the outer rotor, the adhesives were strong enough to keep all the magnets together with the back iron.

Examination of the results of the numerical simulation revealed that although stress concentrated at the edges of the PMs, the maximum stresses were considerably lower than the magnet strength (Fig. 13).

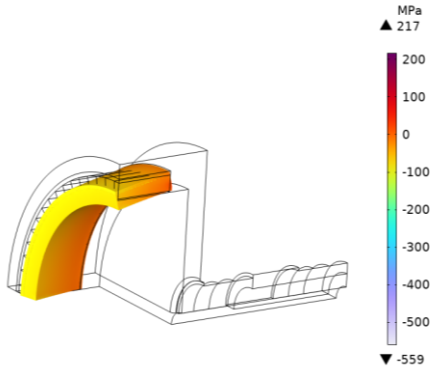

FIGURE 13. Hoop stress at the magnet arrays.

C. C-FIBER SLEEVE DESIGN

The results of the structural FEA analysis showed that a compressive load of 100 MPa was needed to support the structure at the highest speed. This compressive load was achieved by using C-fiber composite materials. The sleeve was made up of 250,000 microfibers and had a total thickness of 5 mm with a width equivalent to the length of the rotor, which was 75 mm. For the FEA formulation, the fiber sleeve was considered a solid cylinder with anisotropic properties, as outlined in Table II. To ensure the contact pressure was around 100 MPa, the artificial overlap method in Abaqus was used to introduce an initial interference of 2 mm between the C-fiber inner surface and the rotor frame's outer surface. This initial interference setup allowed Abaqus to balance the contact pressure and centrifugal load to achieve a converged stress state. It is worth noting that the initial interference value of 2 mm was a fictitious value used only in the finite element model to apply compressive stress to the rotor frame.

Fig. 14(a) shows the compressive stress at the external surface of the outer rotor structure, and Fig. 14(b) shows the hoop stress in the sleeve.

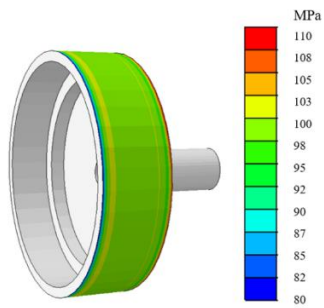

This work is licensed under a Creative Commons Attribution-NonCommercial-NoDerivatives 4.0 License. For more information, see https://creativecommons.org/licenses/by-nc-nd/4

This article has been accepted for publication in IEEE Access. This is the author's version which has not been fully edited and content may change prior to final publication. Citation information: DOI 10.1109/ACCESS.2024.3404410

(a)

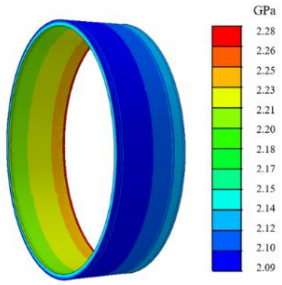

(b)

FIGURE 14. (a) Contact pressure at the outer rotor external surface and (b) hoop stress in the sleeve.

Fig. 14(a) shows a gradient of contact pressure at the outer surface of the rotor, but most of the outer surface shows contact pressure close to 100 MPa. The maximum hoop stress in the C-fiber sleeve was close to 2.28 GPa, which is considerably lower than the yield strength (Table II).

D. EFFECT OF TEMPERATURE

The maximum temperature for the rotor was set at 80°C to prevent demagnetization of the PMs. This was achieved through magnet segmentation, which significantly reduced eddy current loss in the magnets. To maintain the magnet temperature below 80°C [31], air gap cooling was necessary when the high-speed condition was reached. The mechanical properties, such as the modulus of elasticity and Poisson's ratio, did not significantly change at this temperature [32].

E. MAXIMUM SPEED LIMIT OF THE MOTOR

As previously discussed, the C-fiber sleeve plays an essential role in enabling the rotor to achieve mechanical speed while keeping the rotary components intact. The current sleeve design provides a compressive pressure of 100 MPa on the surface of the rotor, which is sufficient for maintaining the rotor's stability. With this sleeve, the motor can reach a maximum speed of 21,000 rpm. However, if the motor were to exceed this speed, the tensile stress in the magnet arrays would exceed the yield limit of 74 MPa, ultimately resulting in permanent deformation of the magnet arrays. Fig. 15 shows the hoop stress map in the magnet array for 20,000 and 21,000 rpm.

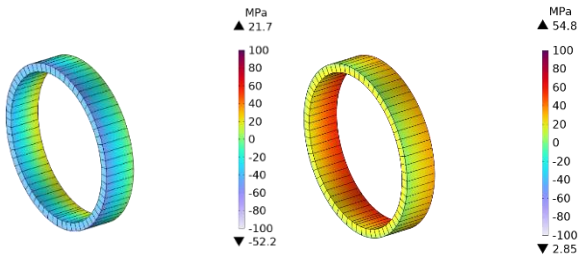

FIGURE 15. Hoop stress on magnet arrays for (a) 20,000 rpm and (b) 21,000 rpm.

V. VIBRATION ANALYSIS

Natural frequency analysis [33], [34], [35] of a rotor involves determining the inherent frequencies at which the rotor tends to vibrate freely. This analysis is important for understanding the dynamic behavior and potential vibration modes of the rotor. For any system with mass m, mechanical stiffness k, and external force f, the governing equation of motion is

$$mu^{\cdot\cdot} + ku = f(t). \tag{4}$$

If the external force were 0 N, the nonzero solution would still exist, and the corresponding solution would be

$$u = Asin(\omega_0 t) + Bcos(\omega_0 t), \tag{5}$$

$$\omega_0 = \sqrt{\frac{k}{m}}, \tag{6}$$

where ω_0 is the natural angular frequency (rad/s) and $\omega_0 = 2\pi f_0$, where f_0 is the natural frequency (Hz). The rotor showed a shift in natural frequencies at 0 rpm, operating speed, and peak speed. The response of a structure is affected by its initial state, and the initial state is affected by the preloading

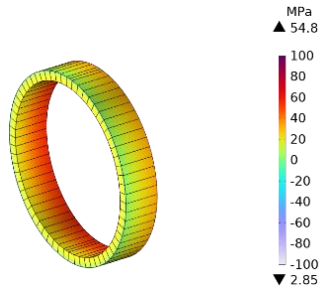

or prestressing applied to the structure prior to the analysis of interest. A prestressed stiffness matrix, $K_{prestressed}$, instead of the original stiffness matrix K of the unloaded structure, is used in the prestressed linear analysis to account for the prestressing effect. When the prestressing subcase is linear and static, the prestressing is captured or defined by a geometric stiffness matrix k_σ, which is based on the stresses of the preloading static subcase. This geometric stiffness matrix is augmented with the original stiffness matrix K to form the prestressed stiffness matrix:

$$K_{prestressed} = K + K_\sigma. \tag{7}$$

Table VI shows the natural frequencies of the cantilever rotor structure at 0, 6,666, and 20,000 rpm at the free- free condition without the C-fiber sleeve. The natural frequency for each mode of vibration increased with increasing rotor speed. Fig. 16 shows each mode of vibration. In mode 1, the greater-mass part tilted front and back, whereas in mode 2, the greater-mass part rotated with respect to the vertical axis. Mode 3 shows the lateral movement of the greater-mass part, and mode 4 shows the 4-point vibration of the greater-mass part.

TABLE VI
NATURAL FREQUENCIES (HZ) FOR DIFFERENT MODES AT DIFFERENT SPEEDS (WITHOUT THE C-FIBER SLEEVE) FOR THE CANTILEVER ROTOR

Modes	0 rpm	Rated speed	Peak speed
Mode 1	400	415.83	483.33

This work is licensed under a Creative Commons Attribution-NonCommercial-NoDerivatives 4.0 License. For more information, see https://creativecommons.org/licenses/by-nc-nd/4

This article has been accepted for publication in IEEE Access. This is the author's version which has not been fully edited and content may change prior to final publication. Citation information: DOI 10.1109/ACCESS.2024.3404410

Mode 2	401	416.46	483.92
Mode 3	836	834.35	845
Mode 4	1,743	1,706.3	1,761

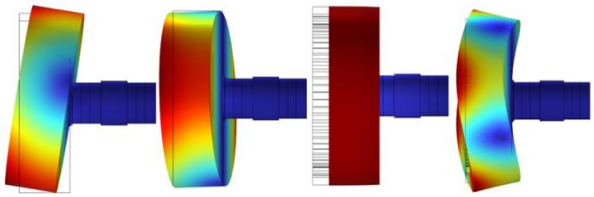

(a) (b) (c) (d)

FIGURE 16. Modes of vibration: (a) mode 1, (b) mode 2, (c) mode 3, and (d) mode 4 for the cantilever design.

Table VII shows the natural frequencies of the simply supported structure at 0, 6,666, and 20,000 rpm at free-free condition without the C-fiber sleeve. Fig. 17 shows the modes of vibration at the corresponding natural frequencies.

TABLE VII
NATURAL FREQUENCIES (HZ) FOR DIFFERENT MODES AT DIFFERENT SPEEDS (WITHOUT THE C-FIBER SLEEVE) FOR THE SIMPLY SUPPORTED ROTOR

Modes	0 rpm	Rated speed	Peak speed
Mode 1	566	558	569
Mode 2	2,089	2,071	2,070
Mode 3	2,208	2,198	2,214
Mode 4	2,766	2,725	2,779

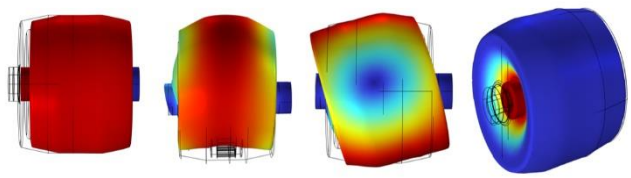

(a) (b) (c) (d)

FIGURE 17. Modes of vibration: (a) mode 1, (b) mode 2, (c) mode 3, and (d) mode 4 for the simply supported design.

In Fig. 17, modes 1 and 4 demonstrate the compression of the rotor's side plate, mode 2 shows bending, and mode 3 shows the rotor tilting. To investigate the influence of temperature on the rotor's natural frequency and modal shapes, an FEA analysis was conducted on the rotor at 80°C. Because the mechanical material properties did not exhibit any significant changes [34], the natural frequency and vibration modes were not notably affected.

VI. FORCED FREQUENCY ANALYSIS

The natural frequency analysis described in the previous section provided helpful information on the system's natural frequencies. However, operating the system at these frequencies could cause mechanical resonance of the rotor. At resonance points, the rotor may undergo large oscillations that can lead to mechanical vibrations, affecting the design air gap between the stator and rotor. Furthermore, natural frequency analysis provided only the modes of vibration and corresponding frequencies, not the physical displacements of the rotor. To understand the physical displacements, forced frequency analysis was performed to measure the maximum displacements at the resonance points. A harmonic point excitation force of 100 N was introduced at the inner surfaces of the magnets in both tangential and radial directions. The torque ripple was assumed to be the excitation source, and the perturbation's magnitude was derived from a 10% torque ripple assumption. Electromagnetic FEA revealed that the motor torque ripple had a fundamental frequency of 60 times the rotor mechanical frequency.

Fig. 18 shows the maximum displacement of the cantilever rotor with the C-fiber sleeve at 20,000 rpm for 100 N harmonic excitation with no damping and with 1% and 5% isotropic damping. The natural frequency for the cantilever design was 373 Hz at 20,000 rpm with 100 MPa preloading by the C-fiber sleeve.

Interestingly, with preloading induced by the C-fiber sleeve, the natural frequency decreased from the natural frequency without the C-fiber sleeve. Resonance occurred close to the mode 1 natural frequency without damping, and the corresponding vibration amplitude was approximately 0.1 mm. However, with 1% damping displacement, it decreased by about 2 times, and with 5% damping, it fell by about 10 times.

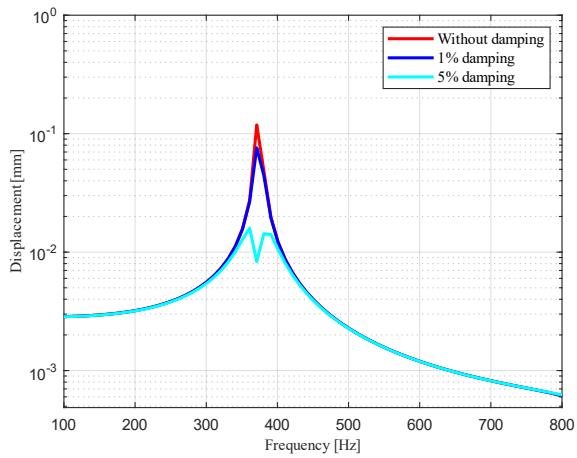

FIGURE 18. Displacement of the cantilever rotor at 20,000 rpm at different damping conditions.

Fig. 19 depicts the maximum displacement of a supported rotor with a C-fiber sleeve under 100 N harmonic excitation at 20,000 rpm without damping and with 1% and 5% isotropic damping. At 20,000 rpm, the fundamental frequency was 565 Hz, and the C-fiber sleeve had a preloading of 100 MPa. The rotor experienced resonance close to the 565 Hz frequency, where the displacement amplitude was approximately 0.1 mm without damping. However, when 1% damping was added, the displacement was reduced by a factor of 10 compared with the undamped rotor. With 5% damping, the displacement was reduced by a factor of approximately

This work is licensed under a Creative Commons Attribution-NonCommercial-NoDerivatives 4.0 License. For more information, see https://creativecommons.org/licenses/by-nc-nd/4

This article has been accepted for publication in IEEE Access. This is the author's version which has not been fully edited and content may change prior to final publication. Citation information: DOI 10.1109/ACCESS.2024.3404410

100. Table VII shows the amplitiudes of displacements at resonance points.

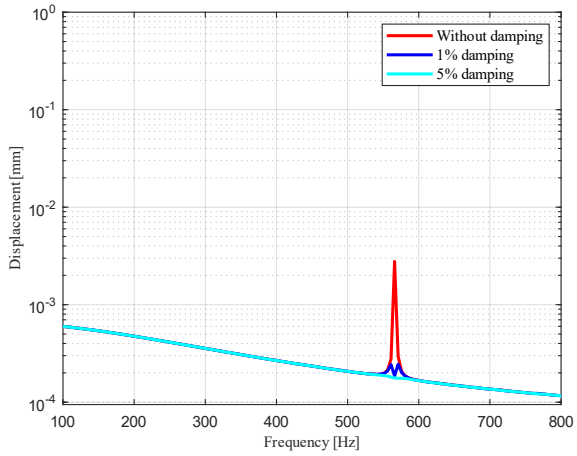

FIGURE 19. Displacement of the simply supported rotor at 20,000 rpm at different damping conditions.

Table VIII shows that with even 1% damping, the magnitude of rotor displacement was less than 0.1 mm, which is negligible. That magnitude of rotor displacement would not interfere with the air gap, and no changes in motor performance and efficiency were expected.

TABLE VIII
DISPLACEMENT OF THE ROTOR STRUCTURE AT RESONANCE FREQUENCY FOR DIFFERENT DAMPING CONDITIONS

	Cantilever design (mm)	Simply supported design (mm)
No damping	0.12	0.005
1% damping	0.08	0.0006
5% damping	0.007	0.00005

VII. ROTODYNAMIC ANALYSIS OF THE ROTOR

Rotor dynamics is the study of the behavior of rotating systems, specifically the vibration and stability characteristics of rotors. When analyzing rotors, several essential factors need to be considered, including rotor geometry, mass distribution, shaft stiffness, bearing characteristics and stiffness, external loads, and critical speed. The critical speed of a rotor is the rotational speed at which resonance occurs, leading to excessive vibrations, increased stresses, and instability. The critical speed of a rotor depends on its geometry, mass distribution, and bearing stiffness. In this study, FEA was used to determine the critical speed of the rotor for different bearing stiffnesses.

The analytical formulation of the critical speed of a rotor is given by

$$critical\ speed = \frac{k}{2\pi} \times \sqrt{\left(\frac{C}{m}\right)}, \qquad (8)$$

where k is a constant related to the mode shape, C is rotor stiffness, and m is rotor mass.

This formula assumes simple bending mode and ignores gyroscopic motion. A Campbell diagram was generated with FEA. A Campbell diagram, also known as a stability or frequency map, is a graphical representation of the critical speeds and corresponding mode shapes of a rotor system. It helps to visualize the rotor's stability regions and identify potential resonance conditions. Figs. 20 and 21 show the Campbell diagrams for the cantilever rotor and simply supported rotor, respectively, for four angular contact bearings (GMN bearing, part number: HY KH 61912 C TA) with 60 mm bore diameter, 13 mm width, 32 ceramic balls (Si_3N_4), and grease lubrication. (In Figs. 20 and 21, FL stands for forward whirl, and BL stands for backward whirl.) The bearings can operate up to 27,000 rpm. The bearing stiffness was considered as 163 N/µm. Though bearing stiffness is a function of rotating speed, for this study, the worst-case scenario was considered. In the best-case scenario, the stiffness would be greater, approximately 212 N/µm. At that stiffness, the critical speed would shift further from the rated speed.

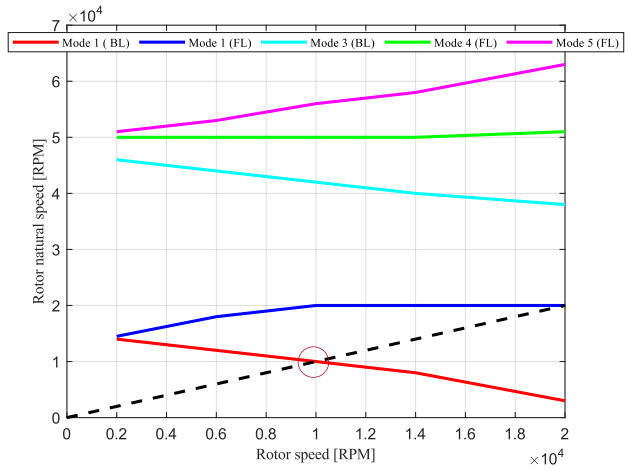

FIGURE 20. Campbell diagram for the cantilever rotor (bearing stiffness: 163 N/µm).

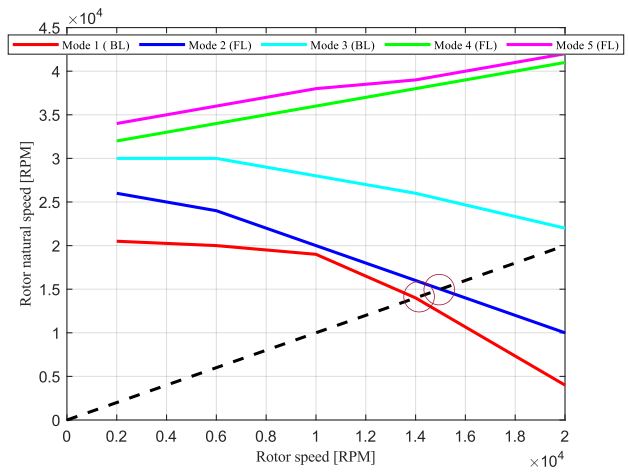

This work is licensed under a Creative Commons Attribution-NonCommercial-NoDerivatives 4.0 License. For more information, see https://creativecommons.org/licenses/by-nc-nd/4

This article has been accepted for publication in IEEE Access. This is the author's version which has not been fully edited and content may change prior to final publication. Citation information: DOI 10.1109/ACCESS.2024.3404410

FIGURE 21. Campbell diagram for the simply supported rotor (bearing stiffness: 163 N/μm).

Fig. 20 shows that the critical speed for the cantilever rotor was 10,000 rpm, and Fig. 21 shows that the critical speeds for the simply supported rotor were approximately 14,000 and 15,000 rpm. Increasing the stiffness by a factor of 1.3 would increase the critical speed by approximately 1,000 rpm for both rotors. Considering the rated speed of 6,666 rpm and the peak speed of 20,000 rpm, the critical speed was 4,000 rpm higher than the rated speed for the cantilever design and 8,000 rpm higher for the simply supported design. For safe operation, the peak speed needs to be set at 10,000 rpm for the cantilever design and at 15,000 rpm for the simply supported design. If the rotor still needs to operate at 20,000 rpm, sweeping faster through the critical speed could reduce the vibrations.

VIII. VALIDATION

Because most of the work in this study was based on FEA simulations, to validate the methodology, natural frequency and rotodynamic results from [36] were reproduced. Yu et al. [36] designed a cantilever rotor for 15,000 rpm application. Fig. 22 shows this design and the mode of vibration at 582 Hz, and Fig. 23 shows a Campbell diagram for the design.

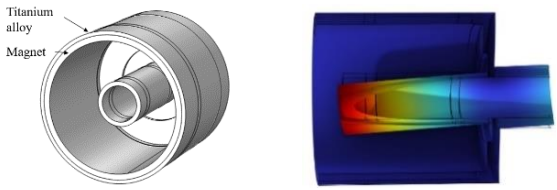

(a) (b)

FIGURE 22. (a) Cantilever design from [36] used for validation and (b) mode of vibration at 582 Hz.

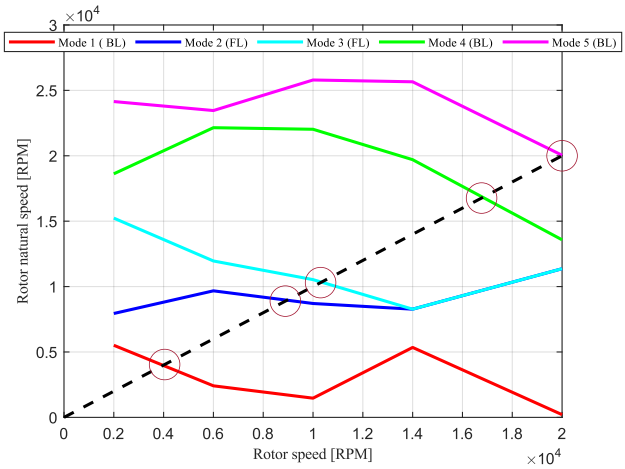

FIGURE 23. Campbell diagram for the design from [24].

The natural frequency corresponding to mode 1 was 582 Hz, whereas the natural frequency derived by [24] was 598 Hz (a less than 5% error margin). The critical speed for the design from [24] was 12,000 rpm, and the critical speed reproduced by the present study for the same design was 10,000 rpm, a 20% error margin. In the present study, four other critical points were derived: at 4,000 rpm, approximately 9,000 rpm, 17,000 rpm, and one close to 20,000 rpm.

IX. GENERAL DESIGN GUIDELINE

The design process for high-speed motors begins with calculating the rotor diameter based on the maximum allowable tip speed. Once the rotor diameter and cooling method are determined, the stack length is calculated from the air-gap shear stress assumption. The appropriate stator slot / rotor pole combination is then selected, considering fundamental frequency limitations, winding arrangement, and cogging torque requirements. FEA is used to compare the candidate slot-pole combinations, and the one that meets the performance requirements is down-selected. Then, a detailed design is conducted, which determines dimensional parameters, the number of turns, current rating, and PM volume. A previous work by the authors [37] provides a detailed description of the electromagnetic design of this motor. To conduct the mechanical design of high-speed motors, the first step following the electromagnetic design is conducting a spin analysis and checking the hoop stress and von Mises stress map of the rotor parts. These stresses are then compared with the strength of the corresponding components. PMs generally have lower tensile strength and higher compressive strength, so keeping the magnets under compression rather than tension is essential. At higher speeds, a C-fiber sleeve can wrap around the rotor, providing a compressive load and balancing the centrifugal force, which is tensile. Besides structural integrity, high-speed motors face challenges due to mechanical vibrations. The initial modal analysis provides the system's natural frequency and corresponding vibration modes, and forced frequency analysis provides the displacements at resonance points. Rotodynamic analysis provides the critical speeds that need to be avoided. All these analyses must be conducted to achieve a sustainable mechanical design for high-speed motors.

X. CONCLUSION AND FUTURE DIRECTION

In this study, the goal was to develop a framework to design an electric motor for integrated electric drive application that satisfies the technical goal set by US DRIVE 2025. To reach the power density of 33 kW/L for electric drive, the inverter was placed inside the stator bore, which necessitated an outer rotor motor design. Two outer rotor designs were proposed and tested by FEA. Both designs showed deformation beyond the acceptable limit at peak speed, 20,000 rpm. To sustain the hoop stress, a C-fiber sleeve was proposed and wrapped around the rotors, which kept the hoop stress under the yield strength of rotor steel. Modal analysis and forced frequency analysis were performed for both designs to extract the natural frequencies and the maximum vibration amplitudes at resonant conditions. Campbell diagrams were generated by rotodynamic analysis for both the rotors.

This work is licensed under a Creative Commons Attribution-NonCommercial-NoDerivatives 4.0 License. For more information, see https://creativecommons.org/licenses/by-nc-nd/4

This article has been accepted for publication in IEEE Access. This is the author's version which has not been fully edited and content may change prior to final publication. Citation information: DOI 10.1109/ACCESS.2024.3404410

The results show that, in terms of structural stress and vibrations, a simply supported rotor design has better mechanical performance because the maximum stress is lower and fundamental natural frequency and critical speed are higher than in the cantilever design. However, in terms of volume and weight, the cantilever design has a significant advantage (Table IV) and has larger space to accommodate the stator and inverter.

ACKNOWLEDGMENT

The authors thank Susan Rogers of DOE for her support and guidance. The authors also thank Jon Wilkins for the CAD designs, Mostak Mohammad and Shajjad Chowdhury for technical guidance, and Emma Shamblin for editing.

REFERENCES

[1] D. Gerada, A. Mebarki, N. L. Brown, C. Gerada, A. Cavagnino, and A. Boglietti, "High-speed electrical machines: technologies, trends, and developments," *IEEE Trans. Industrial Electron.*, vol. 61, no.6, pp. 2946–2959, 2014.

[2] F. Zhang, G. Du, T. Wang, G. Liu, and W. Cao, "Rotor retaining sleeve design for a 1.12-MW high-speed PM machine," *IEEE Trans. Industry Appl.*, vol. 51, no. 5, pp. 3675–3685, 2015.

[3] M. Alibeik and E. C. dos Santos, "High-torque electric machines: state of the art and comparison," *Machines*, vol. 10, no. 8, 2022.

[4] O. Tosun and N. F. O. Serteller, "The Design of the Outer-Rotor Brushless DC Motor and an Investigation of Motor Axial-Length-to-Pole-Pitch Ratio," *Sustain.*, vol. 14, no. 19, 12743, 2022, doi: 10.3390/su141912743.

[5] K. Toker, O. Tosun, N. F. O. Serteller, and V. Topuz, "Design, Optimization and Experimental Study of Axial and Hub BLDC Motors in-Wheel Application for Light Electric Vehicles," *2022 IEEE 21st Mediterranean Electrotech. Conf.* (MELECON), Palermo, Italy, pp. 354–359, 2022, doi: 10.1109/MELECON53508.2022.9842975.

[6] Z. T. Ran, Z. Q. Zhu, F. R. Wei, and E. Cetin, "Comparative Study of Yokeless Dual-rotor and External-Rotor Radial-Flux Fractional-Slot PM Machines," in *2022 Int. Conf. Electrical Machines*, pp. 1913–1919.

[7] Y. Chen, R. Sanchez, A. Yoon, and K. S. Haran, "Mechanical design considerations of an 'ironless,' high-specific-power electric machine," *IEEE Trans. Transp. Electrific.*, vol. 3, no. 4, pp. 855–863, 2017.

[8] S. Koyuncu, U. Tuncer, A. Dalcali, and S. Oncu, "External rotor 6/8 switched reluctance motor design for E-bike," in *10th IEEE Int. Conf. Renewable Energy Research and Applications*, 2021, pp. 131–135.

[9] R. Sanchez, A. Yoon, X. Yi, Y. Chen, L. Zheng, and K. Haran, "Mechanical validation of high power density external cantilevered rotor," presented at the 2017 IEEE International Electric Machines and Drives Conference, Aug. 2017.

[10] A. Borisavljevic, H. Polinder, and J. A. Ferreira, "On the speed limits of permanent-magnet machines," *IEEE Trans. Industrial Electron.*, vol. 57, no. 1, pp. 220–227, Jan. 2010.

[11] N. Bianchi, S. Bolognani, and F. Luise, "Potentials and limits of high-speed PM motors," *IEEE Trans. Industry Appl.*, vol. 40, no. 6, pp. 1570–1578, 2004.

[12] G. Chu, R. Dutta, M. F. Rahman, H. Lovatt, and B. Sarlioglu, "Analytical calculation of maximum mechanical stress on the rotor of interior permanent-magnet synchronous machines," *IEEE Trans. Industry Appl.*, vol. 56, no. 2, pp. 1321–1331, 2020.

[13] T. Nagaoka, M. Takemoto, and S. Ogasawara, "Rotor design of a 150kW 6,000rpm/25,000rpm high speed induction motor for testing equipment of EV/HEV traction motors," in *18th Int. Conf. Electrical Machines and Systems*, 2016, pp. 163–168.

[14] S. Barrans, L. Mallin, S. Barrans, and L. Mallin, "Mechanical design of rotors with surface mounted permanent magnets," *Electric Machines for Smart Grids Applications – Design, Simulation and Control*, 2018.

[15] E. Schubert and B. Sarlioglu, "Mechanical design method for a high-speed surface permanent magnet rotor," in *2016 IEEE Energy Conversion Congr. and Expo. (ECCE) Proc.*, doi: 10.1109/ECCE.2016.7855239.

[16] US DRIVE, Electrical and Electronics Technical Team Roadmap, 2017. [Online]. Available: https://www.energy.gov/eere/vehicles/articles/us-drive-electrical-and-electronics-technical-team-roadmap.

[17] W. Q. Wang, Y. Li, D. J. Huan, X. D. Chen, H. Q. Liu, Y. R. Li *et al.*, "Research on stress design and manufacture of the fiber-reinforced composite sleeve for the rotor of high-speed permanent magnet motor," *Energies*, vol. 15, no. 7, 2022.

[18] A. Borisavljevic, H. Polinder, and J. Ferreira, "Enclosure design for a high-speed permanent magnet rotor," presented at the 5th IET Int. Conf. Power Electronics, Machines and Drives, July 26, 2010.

[19] Y. Wang, Z. Q. Zhu, J. H. Feng, S. Y. Guo, Y. F. Li, and Y. Wang, "Rotor stress analysis of high-speed permanent magnet machines with segmented magnets retained by carbon-fibre sleeve," *IEEE Trans. Energy Convers.*, vol. 36, no. 2, pp. 971–983, 2021.

[20] Y. Yu *et al.*, "Rotordynamic assessment for an inside out, high speed permanent magnet synchronous *motor*," in *Proc. 2020 Int. Conf. Electrical Machines*, Aug. 2020, pp. 529–535.

[21] T. Balachandran, S. Srimmana, A. Anderson, X. Yi, N. Renner, and K. S. Haran, "Assembly and qualification of a slotless stator assembly for a MW-class permanent magnet synchronous machine," in *2020 AIAA/IEEE Electric Aircraft Technologies Symp. (EATS)*, pp. 1–10.

[22] S. Selmaˇ, S. Selmačorovi´c, and D. Miljavec, "Modal analysis and rotor-dynamics of an interior permanent magnet synchronous motor: An experimental and theoretical study," *Appl. Sci.*, vol. 10, no. 7, p. 5881, 2020, doi: 10.3390/APP10175881.

[23] Z. Li, Q. Chen, F. Yue, and Q. Wang, "Analysis of the rotor dynamics characteristics of multi-degree-of-freedom permanent magnet synchronous motor," *J. Low Freq. Noise Vib. and Act. Control*, vol. 38, no. 2, pp. 352–362, 2019, doi: 10.1177/1461348419830211.

[24] T. W. Lee and D. K. Hong, "Rotor design, analysis and experimental validation of a high-speed permanent magnet synchronous motor for electric turbocharger," *IEEE Access*, vol. 10, pp. 21955–21969, 2022, doi: 10.1109/ACCESS.2022.3152525.

[25] G. J. Su and L. Tang, "A segmented traction drive system with a small dc bus capacitor," in *2012 IEEE Energy Conversion Congr. and Expo. (ECCE)*, pp. 2847–2853, doi: 10.1109/ECCE.2012.6342375.

[26] A. Błachut, T. Wollmann, M. Panek, M. Vater, J. Kaleta, J. Detyna, S. Hoschützky, and M. Gude, "Influence of fiber tension during filament winding on the mechanical properties of composite vessels," *Composite Struct.*, 116337, 2022.

[27] "Neodymium Sintered - Standard Grades." [Online]. Available: https://bakkermagnetics.com/wp-content/uploads/2019/01/neodymium_sintered_-_standard_grades_0.pdf. Accessed on: Aug. 2, 2023.

[28] "Dexter Magnetic Technologies." [Online]. Available: https://www.dextermag.com/.

[29] V. Rallabandi, M. Mohammad, H. Barua, S. Chowdhury, B. Ozpineci, J. Wilkins, L. Lin, B. Kekelia, and J. E. Cousineau, "An integrated traction drive with a high speed surface permanent magnet external rotor motor for electric vehicles," in *2023 IEEE Energy Conversion Congr. and Expo. (ECCE)*, pp. 4140–4146, doi: 10.1109/ECCE53617.2023.10362087,

[30] Equilibrium." [Online]. Available: https://www.continuummechanics.org/equilibrium.html. Accessed on: Jan. 22, 2024.

[31] V. Rallabandi, M. Mohammad, H. Barua, S. Chowdhury, B. Ozpineci, J. Wilkins, L. Lin, B. Kekelia, and J. E. Cousineau, "An

This work is licensed under a Creative Commons Attribution-NonCommercial-NoDerivatives 4.0 License. For more information, see https://creativecommons.org/licenses/by-nc-nd/4

This article has been accepted for publication in IEEE Access. This is the author's version which has not been fully edited and content may change prior to final publication. Citation information: DOI 10.1109/ACCESS.2024.3404410

integrated traction drive with a high speed surface permanent magnet external rotor motor for electric vehicles," in *2023 IEEE Energy Conversion Congr. and Expo. (ECCE)*, pp. 4140–4146, doi: 10.1109/ECCE53617.2023.10362087.

[32] "Metals and Alloys - Young's Modulus of Elasticity." [Online]. Available: https://www.engineeringtoolbox.com/young-modulus-d_773.html. Accessed on: Jan. 28, 2024.

[33] J. Zhao, Z. Wang, H. Liu, F. Ning, X. Hong, J. Du, and M. Yu, "Modal analysis and structure optimization of permanent magnet synchronous motor," *IEEE Access*, vol. 8, pp. 151856–151865, 2020, doi: 10.1109/ACCESS.2020.3017679.

[34] S. Selmaˇ, S. Selmačorovi´c, and D. Miljavec, "Modal analysis and rotor-dynamics of an interior permanent magnet synchronous motor: An experimental and theoretical study," *Appl. Sci*., vol. 10, no. 17, p. 5881, 2020, doi: 10.3390/APP10175881.

[35] C. Wang and J. C. S. Lai, "Vibration analysis of an induction motor," *J. Sound and Vib*., vol. 224, no. 4, pp. 733–756, 1999, doi: 10.1006/JSVI.1999.2208.

[36] Y. Yu, S. Sirimanna, K. Haran, T. Clydesdale, B. Sharos, D. Lubell, and B. Murphy, "Rotordynamic assessment for an inside out, high speed permanent magnet synchronous motor," in *Proc. 2020 Int. Conf. Electrical Machines (ICEM 2020)*, pp. 529–535, doi: 10.1109/ICEM49940.2020.9270695.

[37] T. Raminosoa, R. Wiles, J. E. Cousineau, K. Bennion, and J. Wilkins, "A high-speed high-power-density non-heavy rare-earth permanent magnet traction motor," in *2020 IEEE Energy Conversion Congr. and Expo. (ECCE)*, pp. 61–67, doi: 10.1109/ECCE44975.2020.9235704.

HIMEL BARUA (Member, IEEE) is a research associate at Oak Ridge National Laboratory in the Buildings and Transportation Science Division, Propulsion Science Section, and the Electric Drives Research Group. He received his B.Sc. in mechanical engineering from Bangladesh University of Engineering and Technology in 2011 and received his M.Sc. and Ph.D. in mechanical engineering from The University of Akron, Ohio, in 2016 and 2021, respectively. His research interests include finite element analysis and structural, rotodynamic, and mechanical vibration study of high-speed electric machines as well as thermal management of high-power modules and thermal-fluid flow simulation for different applications.

LIANSHAN LIN was born in Longhai, Fujian Province, China, in 1979. He received his B.S. and M.S. degrees in aerospace engineering from the Beijing University of Aeronautics and Astronautics, China, in 2000 and 2003, respectively. He received his Ph.D. degree in mechanical engineering from Manchester University, United Kingdom, in 2009. Before becoming a staff member at Oak Ridge National Laboratory in 2016, he worked as a postdoc at the University of Minnesota and a postdoc at Oak Ridge National Laboratory for years. His research interests include rotodynamic and structural stress analysis of electric vehicle motors as well as structural materials in nuclear engineering, including high-temperature alloys and graphite.

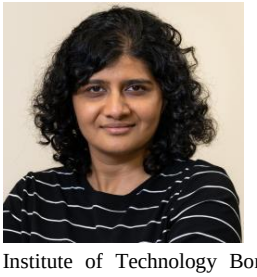

VANDANA RALLABANDI (Senior Member, IEEE) joined Oak Ridge National Laboratory in 2022. Previously, she was a lead engineer with the GE Research Center in Niskayuna, New York. She has also held positions as a postdoctoral researcher with the SPARK Lab, University of Kentucky, Lexington, and as a research engineer at GE Research, Bangalore, India. She received her M.Tech. and Ph.D. degrees from the Indian Institute of Technology Bombay, Mumbai, India, in 2008 and 2013, respectively. Her research interests include electric machines, power electronics drives, renewable energy devices and systems, energy storage, and power systems. She is an associate editor for the *IEEE Transactions on Energy Conversion*.

JONATHAN WILKINS received his dual bachelor's degrees in physics and mathematics from Bethany College in West Virginia in 2002. He also received his associate degrees in mechanical and industrial engineering technologies from Pellissippi State Technical Community College in 2017 and 2018, respectively. He is currently a technical professional at the Vehicle Power Electronics Research Group at Oak Ridge National Laboratory. His focus areas include wireless and plug-in electric vehicle charging systems, power electronic converters, inverters, compact electric motors, and experimental test setup instrumentation and apparatus.

This work is licensed under a Creative Commons Attribution-NonCommercial-NoDerivatives 4.0 License. For more information, see https://creativecommons.org/licenses/by-nc-nd/4

This article has been accepted for publication in IEEE Access. This is the author's version which has not been fully edited and content may change prior to final publication. Citation information: DOI 10.1109/ACCESS.2024.3404410

PRAVEEN KUMAR (Senior Member, IEEE) received his B.Tech. degree in electrical engineering from the National Institute of Technology, Hamirpur, India, in 1998; his M.Tech. degree in energy systems from the Indian Institute of Technology Delhi, India, in 2000; and his Ph.D. degree in electrical machines from the Delft University of Technology, the Netherlands, in 2008. His current research interests include optimizing electrical motors and drives, hybrid and electric vehicles, smart grids, wired charging, and wireless charging of electric vehicles. Dr. Kumar is an active reviewer of many journals, including the *IEEE Transactions on Industrial Electronics*, *IEEE Transactions on Energy Conversion*, and *IEEE Transactions on Magnetics*.

BURAK OZPINECI (Fellow, IEEE) received his B.S. degree in electrical engineering from Orta Dogu Technical University, Ankara, Turkey, in 1994 and his M.S. and Ph.D. degrees in electrical engineering from the University of Tennessee, Knoxville, in 1998 and 2002, respectively. In 2001, he joined the post-master's program with the Power Electronics and Electric Machinery Group at Oak Ridge National Laboratory (ORNL). He became a full-time research and development staff member in 2002, the group leader of the Power and Energy Systems Group in 2008, and the group leader of the Power Electronics and Electric Machinery Group in 2011. Presently, he is a corporate fellow at ORNL serving as the section head for the Vehicle and Mobility Systems Research Section. He is also a joint faculty with the Bredesen Center, the University of Tennessee.

This work is licensed under a Creative Commons Attribution-NonCommercial-NoDerivatives 4.0 License. For more information, see https://creativecommons.org/licenses/by-nc-nd/4